

PROPAGATION AND DISPERSION OF SAUSAGE WAVE TRAINS IN MAGNETIC FLUX TUBES

R. OLIVER¹, M. S. RUDERMAN^{2,3}, AND J. TERRADAS¹¹ Departament de Física, Universitat de les Illes Balears, E-07122 Palma de Mallorca, Spain; ramon.oliver@uib.es² School of Mathematics and Statistics, University of Sheffield, Hicks Building, Hounsfield Road, Sheffield S3 7RH, UK³ Space Research Institute (IKI), Russian Academy of Sciences, Moscow 117997, Russia

Received 2015 February 4; accepted 2015 April 18; published 2015 June 8

ABSTRACT

A localized perturbation of a magnetic flux tube produces wave trains that disperse as they propagate along the tube, where the extent of dispersion depends on the physical properties of the magnetic structure, on the length of the initial excitation, and on its nature (e.g., transverse or axisymmetric). In Oliver et al. we considered a transverse initial perturbation, whereas the temporal evolution of an axisymmetric one is examined here. In both papers we use a method based on Fourier integrals to solve the initial value problem. We find that the propagating wave train undergoes stronger attenuation for longer axisymmetric (or shorter transverse) perturbations, while the internal to external density ratio has a smaller effect on the attenuation. Moreover, for parameter values typical of coronal loops axisymmetric (transverse) wave trains travel at a speed 0.75–1 (1.2) times the Alfvén speed of the magnetic tube. In both cases, the wave train passage at a fixed position of the magnetic tube gives rise to oscillations with periods of the order of seconds, with axisymmetric disturbances causing more oscillations than transverse ones. To test the detectability of propagating transverse or axisymmetric wave packets in magnetic tubes of the solar atmosphere (e.g., coronal loops, spicules, or prominence threads) a forward modeling of the perturbations must be carried out.

Key words: Sun: corona – Sun: magnetic fields – Sun: oscillations

Supporting material: animation

1. INTRODUCTION

The solar corona supports a rich variety of wave phenomena whose main features are determined by the magnetic field and plasma structuring. For our purposes it is important to distinguish between different wave manifestations such as driven and impulsively excited perturbations. Driven waves are often caused by a continuous, periodic exciter at the photospheric or chromospheric level and propagate away from the place where they are generated. This is the case, for example, of waves propagating upwards along spicules (Okamoto & De Pontieu 2011; De Pontieu et al. 2012) or along the coronal magnetic field (Tomczyk et al. 2007; Tomczyk & McIntosh 2009). The disturbances propagating in filament threads observed by Lin et al. (2007) and Okamoto et al. (2007) are probably representative of driven waves too, although the exciting agent is not clear in this case. Some rapidly propagating quasi-periodic coronal disturbances (Liu et al. 2011, 2012; Shen & Liu 2012; Shen et al. 2013) also seem to be caused by a continuous driver that in this case is associated to a flare or the initiation of a coronal mass ejection. For a modeling of these events see Ofman et al. (2011). We also mention in passing the EUV periodic disturbances propagating along coronal loops with velocities typically on the order of 100 km s^{-1} and periods in the range 2–10 minutes. The similarity between the observed phase speed and the local sound speed has motivated associating these events to propagating slow magnetoacoustic waves (for some reviews, see de Moortel 2009; de Moortel & Nakariakov 2012). Sunspot oscillations can also result from a continuous excitation (Bogdan & Judge 2006).

When a magnetic flux tube (e.g., spicule, coronal loop, or prominence thread) is subject to a periodic driving it shows a distinct response. An axisymmetric driver that periodically compresses and expands the tube at one position leads to the

propagation of a sausage-type perturbation (see Figure 1(a)). A periodic transverse shaking of the tube results in a kink-type perturbation by which the tube boundary acquires the shape of a snake (see Figure 1(a) of Oliver et al. 2014, hereafter Paper I). A torsional driver leads to Alfvén wave propagation along the tube with no apparent modification of its boundary.

On the other hand, an impulsive energy release can lead to both standing and propagating disturbances. The transverse coronal loop oscillations studied by Aschwanden et al. (1999) and Nakariakov et al. (1999) constitute a good example of the first type of phenomenon, for which there are many observational studies in the literature. For recent observations using the Atmospheric Imaging Assembly on board the *Solar Dynamics Observatory*, see Nisticò et al. (2013) and Anfinogentov et al. (2013). Our interest in this work is in the second type of event, i.e., a magnetic flux tube perturbed by a sudden, localized expansion or compression such as that of Figure 1(b) (see also Figure 1(b) of Paper I for a localized transverse excitation). In a dispersive medium, such initial pulse disperses and transforms into a wave train that induces quasi-periodic plasma oscillations with a range of periods (rather than the single-period oscillations of driven propagating waves or standing oscillations). Hence, the time signal (e.g., Doppler shift or spectral line intensity) collected at a given position shows a characteristic “tadpole” shape in its wavelet diagram (e.g., Nakariakov et al. 2004; Jelínek and Karlický 2010). The important difference between driven and impulsively excited waves, then, is that the first ones have the period of the driving agent, whereas the second ones display a continuous variation of the period that depends on the size of the initial perturbation and the physical properties of the medium.

Several observations of quasi-periodic oscillations have been ascribed to the dispersive behavior of propagating wave packets. Williams et al. (2001, 2002) and Katsiyannis et al.

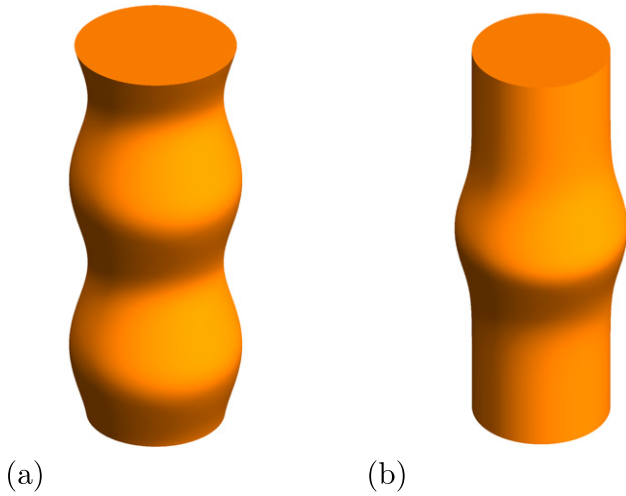


Figure 1. Shape of the boundary of a uniform cylindrical magnetic flux tube subject to (a) a fast sausage normal mode perturbation and (b) a localized axisymmetric perturbation.

(2003) used the Solar Eclipse Corona Imaging System to record white light and coronal green line images of the solar corona during a solar eclipse. They studied the intensity variations in the vicinity of an active region and detected periodic variations with period in the range 4–7 s that propagate through the loop apex with a speed of 2100 km s^{-1} . The wavelet spectra of signals at different points along the wave path display the “tadpole” shape mentioned above. This wavelet feature is also present in solar decimetric radio bursts (Mészáros et al. 2009, 2011; Karlický et al. 2013) and in radio sources lying in a magnetic fan structure (Mészáros et al. 2013). The quasi-periodic, rapidly propagating wave trains observed by Yuan et al. (2013) and Nisticò et al. (2014) are possibly caused by a sudden energy release that excites fast magnetoacoustic wave packets whose posterior propagation is guided by the magnetic field. These events possess propagation speeds well in excess of 600 km s^{-1} , i.e., of the order of the coronal Alfvén speed, and periods in the range 40–80 s.

The impulsive excitation of fast MHD waves, and their subsequent evolution as an oscillatory wave train, has been addressed for different magnetic structures: fast sausage wave trains in a coronal slab (Murawski & Roberts 1993a, 1993b; Nakariakov et al. 2004, 2005, 2012; Jelínek and Karlický 2010; Mészáros et al. 2014), in a current sheet (Jelínek and Karlický 2012; Jelínek et al. 2012; Karlický et al. 2013; Mészáros et al. 2014), and in a magnetic funnel (Pascoe et al. 2013). Impulsively generated fast sausage and kink wave packets in coronal holes have also been studied by Pascoe et al. (2014). Our paper is concerned with the temporal evolution of a concentrated axisymmetric compression or expansion of a uniform, cylindrical magnetic tube; see Figure 1(b). This initial disturbance leads to the propagation of a fast sausage wave train along the tube. The propagation and dispersion of wave packets in magnetic slabs has already been investigated numerically in slab geometry, but not in cylindrical geometry.

In Paper I and in the present work we use a method based on Fourier integrals to solve the partial differential equations (PDEs) that govern the propagation of impulsively excited linear fast MHD perturbations in a magnetic cylinder. This method has several advantages over the direct numerical solution of the governing PDEs. First, to determine the

perturbed state at a given time our method requires no calculations for any previous time. The same applies to the spatial coordinates: the propagation of the impulsively generated wave packet can be studied without solving the PDEs in the spatial range between where the impulse is launched and the final position of interest. There is even no need to integrate the PDEs in the radial direction. To summarize, the present method based on Fourier integrals allows one to select the time and position and to obtain the corresponding physical variables. Second, one can also select which perturbed variables will be calculated; obviously, the required computing time is proportional to the number of computed perturbations. And third, the numerical integration of the MHD equations requires dealing with issues such as implementing the boundary conditions, the stability of the solution, etc. We are unconcerned by these matters because the main numerical calculations of the method used in this work are two quadratures, whose numerical accuracy can be controlled well. The main drawback of our method is the computation of the improper mode contribution, which can be quite time consuming for axisymmetric disturbances.

This is the outline of our paper. Section 2 contains the governing equations of linear fast perturbations in a plasma cylinder in the $\beta = 0$ limit. In Sections 3 and 4 we give a description of fast sausage proper and improper modes, whose spectra are discrete and continuous, respectively. The initial perturbation is used in Section 5 to obtain analytical expressions for the time evolution of the perturbed variables and the results are presented in Section 6.

2. EQUILIBRIUM AND GOVERNING EQUATIONS FOR LINEAR PERTURBATIONS IN A COLD PLASMA CYLINDER

We consider a homogeneous cylindrical magnetic tube embedded in a uniform environment. In this work we use cylindrical coordinates (r, φ, z) , with the z -axis pointing along the cylinder axis. The magnetic field is uniform in the whole space and parallel to the z -axis, and so can be written as $\mathbf{B} = B\hat{e}_z$. The equilibrium density is

$$\rho_0(r) = \begin{cases} \rho_i, & r \leq a, \\ \rho_e, & r > a, \end{cases} \quad (1)$$

where the subscripts “ i ” and “ e ” denote internal and external values, respectively, and a is the tube radius.

Next we consider small perturbations about this equilibrium, governed by the linear, ideal MHD equations, in the cold plasma approximation (Equations (1)–(3) of Ruderman and Erdélyi 2009). In our work \mathbf{v} is the velocity perturbation, $\boldsymbol{\xi}$ the Lagrangian plasma displacement, \mathbf{b} the magnetic field perturbation, $P = Bb_z/\mu_0$ the magnetic pressure perturbation (with μ_0 the magnetic permeability of free space), and ρ the density perturbation. Using Equations (1)–(3) of Ruderman and Erdélyi (2009) it is straightforward to see that, if ξ_z and v_z are initially zero, then they vanish for all times. In addition, perturbations are governed by

$$\rho = \frac{1}{v_A^2} P, \quad (2)$$

$$\frac{\partial^2 \boldsymbol{\xi}}{\partial t^2} = -\frac{1}{\rho_0} \nabla_\perp^2 P + v_A^2 \frac{\partial^2 \boldsymbol{\xi}}{\partial z^2}, \quad (3)$$

$$\mathbf{b}_\perp = B \frac{\partial \boldsymbol{\xi}}{\partial z}, \quad (4)$$

$$P = -\rho_0 v_A^2 \nabla \cdot \boldsymbol{\xi}, \quad (5)$$

$$\mathbf{v} = \frac{\partial \boldsymbol{\xi}}{\partial t}, \quad (6)$$

where we have written $\mathbf{b}_\perp = \mathbf{b} - b_z \hat{\mathbf{e}}_z$ and

$$\nabla_\perp = \nabla - \hat{\mathbf{e}}_z \frac{\partial}{\partial z}.$$

Moreover, v_A is the Alfvén speed, whose values inside and outside the magnetic cylinder are respectively given by

$$v_{Ai}^2 = \frac{B^2}{\mu_0 \rho_i}, \quad v_{Ae}^2 = \frac{B^2}{\mu_0 \rho_e}. \quad (7)$$

In this paper we consider a magnetic tube that is denser than the environment, i.e., $\rho_i > \rho_e$ and $v_{Ai} < v_{Ae}$.

3. PROPER (OR DISCRETE) FAST SAUSAGE MODES

3.1. Eigenfunctions

The eigenfunctions of fast MHD modes in a magnetic cylinder have the azimuthal dependence $\exp(im\varphi)$, with $m = 0$ for sausage modes. Then, the perturbations P , ρ , $\boldsymbol{\xi}$, \mathbf{b} , and \mathbf{v} have no azimuthal dependence and as a consequence the φ -components of Equations (3), (4), and (6) dictate that ξ_φ , b_φ , and v_φ vanish (provided that they are initially zero). In addition, the variables are of the form

$$P(t, r, \varphi, z) = \hat{P}(r) \exp[i(-\omega t + kz)], \quad (8)$$

and similarly for ρ , ξ_r , b_r , and v_r .

It is straightforward to obtain the function $\hat{P}(r)$ for proper fast sausage modes (i.e., with $kv_{Ai} < \omega < kv_{Ae}$) and so the procedure is not given here. The solution to Equations (3) and (5) regular at $r = 0$ and that does not diverge as $r \rightarrow \infty$ is

$$\hat{P}(r) = \begin{cases} C_i J_0(k_i r), & r \leq a, \\ C_e K_0(\kappa_e r), & r \geq a, \end{cases} \quad (9)$$

where C_i and C_e are two constants, J_m is the Bessel function of the first kind and order m , and K_m is the modified Bessel function of the second kind and order m . Moreover,

$$k_i^2 = \frac{\omega^2 - k^2 v_{Ai}^2}{v_{Ai}^2}, \quad (10)$$

$$\kappa_e^2 = -\frac{\omega^2 - k^2 v_{Ae}^2}{v_{Ae}^2}. \quad (11)$$

It is important to mention that when using these equations to determine the radial wavenumbers, the positive value is taken, i.e., $k_i > 0$, $\kappa_e > 0$. An algebraic expression for C_i and C_e is obtained by imposing the continuity of $\hat{P}(r)$ at $r = a$. The remaining constant can be imposed arbitrarily. Here we use expressions analogous to those of Paper I, that is

$$\begin{aligned} C_i &= \rho_i v_{Ai}^2 K_0(\kappa_e a), \\ C_e &= \rho_e v_{Ae}^2 J_0(k_i a). \end{aligned} \quad (12)$$

Now that the function $\hat{P}(r)$ is determined, all other perturbations can be obtained. We write the expression of the radial plasma displacement because it will be used later,

$$\hat{\xi}_r(r) = \begin{cases} -k_i^{-1} K_0(\kappa_e a) J_1(k_i r), & r \leq a, \\ \kappa_e^{-1} J_0(k_i a) K_1(\kappa_e r), & r \geq a, \end{cases} \quad (13)$$

where we have used the relations (Abramowitz & Stegun 1964)

$$J_0'(x) = -J_1(x), \quad K_0'(x) = -K_1(x). \quad (14)$$

Expressions for the rest of perturbations follow from Equations (2), (4), and (6), that yield

$$\begin{aligned} \hat{\rho} &= \frac{1}{v_A^2} \hat{P}, & \hat{b}_r &= ik B \hat{\xi}_r, \\ \hat{v}_r &= -i\omega \hat{\xi}_r. \end{aligned} \quad (15)$$

3.2. Dispersion Relation, Phase Speed, and Group Velocity

Imposing the continuity of the radial displacement at $r = a$ leads to the dispersion relation for proper fast sausage modes,

$$\frac{J_1(k_i a)}{k_i J_0(k_i a)} + \frac{K_1(\kappa_e a)}{\kappa_e K_0(\kappa_e a)} = 0. \quad (16)$$

In this work the dispersion relation is used to obtain the frequency of a proper mode with a given longitudinal wavenumber, k . Therefore, we often write the frequency as $\omega(k)$.

Moreover, the phase speed and group velocity are defined in the usual manner,

$$c_{ph}(k) = \frac{\omega}{k}, \quad c_g(k) = \frac{\partial \omega}{\partial k}. \quad (17)$$

Although the phase speed is not used in our calculations nor in the interpretation of results, it is also given here because it is an important parameter of proper modes. The main features of ω , c_{ph} , and c_g of proper sausage modes in a magnetic cylinder have been discussed in previous works (e.g., Edwin & Roberts 1983; Roberts et al. 1984; Cally 1986). They are summarized below.

First, we discuss some properties of the eigensolutions for the possible sign combinations of k and ω ; they will be useful when the method of Fourier integrals is applied to the wave propagation problem. It is clear that the two pairs of values (k, ω) and $(-k, -\omega)$ correspond to the same eigenmode, propagating in a given direction along the z -axis. It is obvious that the solutions presented above have this property: if the signs of both k and ω are simultaneously changed, then Equations (10) and (11) show that the internal and external radial wavenumbers are not modified. As a result, these new values of the longitudinal wavenumber and frequency also satisfy the dispersion relation. In other words, if $\omega(k)$ is the frequency of a proper mode, then $-\omega(-k)$ is also a frequency of a proper mode. Using Equations (8), (9), (13), and (15), we see that the perturbations of both modes are identical. Finally, we also have $c_{ph}(k) = c_{ph}(-k)$ and $c_g(k) = c_g(-k)$.

Next let us consider a fixed k : if $\omega(k)$ is a solution to the dispersion relation, then $-\omega(k)$ corresponds to the eigenmode propagating in the opposite direction along the magnetic tube. Again, the two eigenmodes have the same eigenfunctions, but opposite phase speed and group velocity. Thus, in the rest of

this section it is enough to concentrate in $k \geq 0$ and $\omega > 0$. Both positive and negative values of k and ω will be taken into account when deriving the solution to the initial value problem by the method of Fourier integrals (Section 5).

The magnetic cylinder supports an infinite number of fast sausage radial overtones, characterized by the number of nodes of $\xi_r(r)$. All radial overtones have a node at the tube axis, $r = 0$. This is the only node for the fundamental sausage eigenmode. The first overtone has two nodes in the radial direction, etc., and all these nodes are inside the magnetic cylinder. An additional feature of proper fast sausage modes is that they only exist for longitudinal wavenumbers exceeding the cut-off value (Roberts et al. 1984; Nakariakov & Verwichte 2005),

$$k_{cj} = \frac{j_{0j} v_{Ai}}{a \sqrt{v_{Ae}^2 - v_{Ai}^2}}, \quad (18)$$

where j_{0j} is the j th zero (in increasing order) of $J_0(x)$. Here $j = 1, 2, \dots$ correspond to the fundamental fast sausage mode, its first radial overtone, etc.

In Figure 2 the frequency, phase speed, and group velocity of the fundamental fast sausage eigenmode and its first overtones are shown for two values of the density ratio, ρ_i/ρ_e . The dispersion diagram (Figure 2(a)) is rarely found in the literature. It shows that all proper modes, including the fundamental one, have a wavenumber cut off and that their frequency satisfies $kv_{Ai} < \omega < kv_{Ae}$. One can see that increasing the density ratio raises the upper frequency limit kv_{Ae} and so more overtones are present in this diagram. It is worth to mention that linear waves with $kv_{Ae} \leq \omega$ also exist, but instead of discrete values of ω these solutions can have any frequency (see Section 4). Figure 2(b) has been presented many times in other works and so is not discussed here. It is enough to note that the phase speed lies between the internal and external Alfvén speeds. Finally, Figure 2(c) shows the group velocity as a function of k . When the wavenumber approaches its cut-off value from the right, c_g rapidly increases and tends to v_{Ae} , i.e., it tends to 3 and 2 for the red and black lines, respectively. For larger wavenumbers, the group velocity decreases to its minimum and finally increases slowly toward v_{Ai} . In Appendix A we show that the phase speed tends to v_{Ai} from above as $ka \rightarrow \infty$. Moreover, the group velocity tends to v_{Ai} from below for very large wavenumbers. This behavior of c_{ph} and c_g is in agreement with Figures 2(b) and (c).

4. IMPROPER (OR CONTINUOUS) FAST SAUSAGE MODES

When a fixed k is considered, proper modes have discrete frequencies in the range $(-kv_{Ae}, kv_{Ae})$ (see purple dashed lines in Figure 2(a)). Improper mode eigenfunctions can also be expressed in the form of Equation (8), but they can have any frequency in the ranges $(-\infty, -kv_{Ae}]$ and $[kv_{Ae}, \infty)$. Paper I contains a detailed discussion of fast kink improper modes properties. All the arguments presented in Paper I are valid for fast improper sausage modes and so are not repeated here. The total pressure and radial displacement perturbations are given

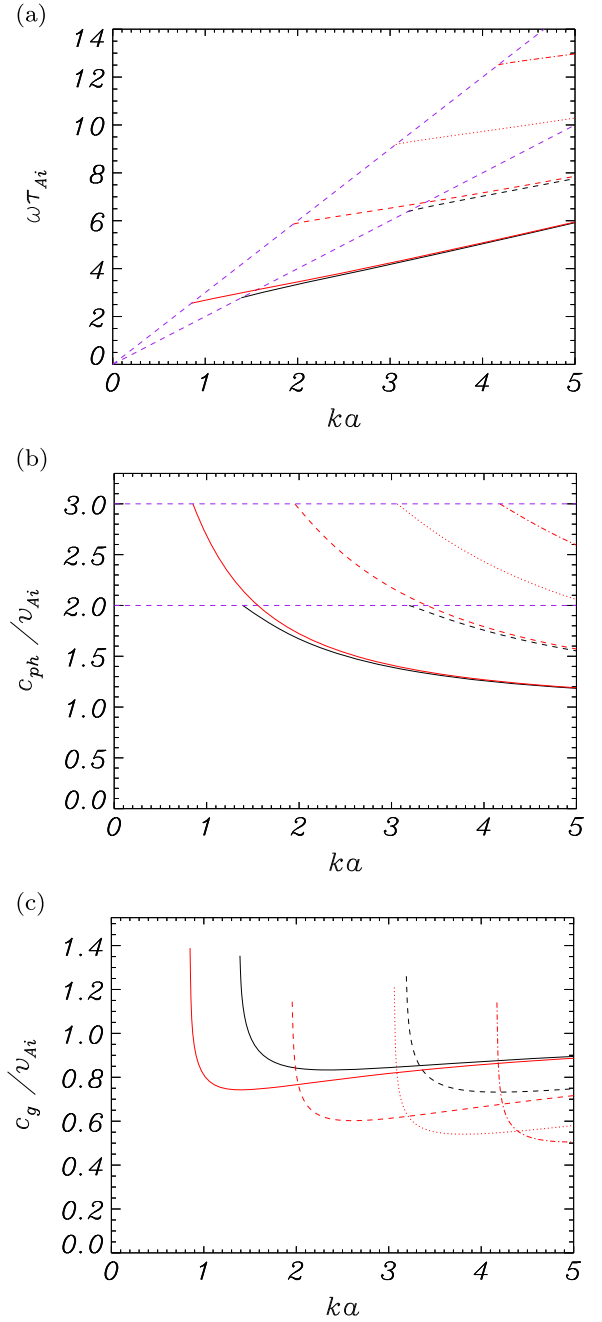


Figure 2. (a) Frequency, (b) phase speed, and (c) group velocity vs. the longitudinal wavenumber for the fundamental fast sausage mode (solid line) and its first overtones in the radial direction (dashed, dotted, and dash-dotted lines). Black and red colors respectively correspond to the equilibrium density ratio $\rho_i/\rho_e = 4$ and 9, i.e., to the Alfvén speed ratio $v_{Ae}/v_{Ai} = 2$ and 3. The purple lines in (a) and (b) correspond to the frequency $\omega = kv_{Ae}$. To obtain the dimensionless quantities, the magnetic cylinder radius (a), Alfvén speed (v_{Ai}), and transit time ($\tau_{Ai} = a/v_{Ai}$) have been used.

by

$$\hat{P}(r) = \begin{cases} \rho_i v_{Ai}^2 a^2 k_e^2 J_0(k_i r), & r \leq a, \\ \rho_e v_{Ae}^2 a^2 k_e^2 [C_J J_0(k_e r) + C_Y Y_0(k_e r)], & r \geq a, \end{cases} \quad (19)$$

$$\hat{\xi}_r(r) = \begin{cases} -a^2 k_e^2 k_i^{-1} J_1(k_i r), & r \leq a, \\ -a^2 k_e [C_J J_1(k_e r) + C_Y Y_1(k_e r)], & r \geq a, \end{cases} \quad (20)$$

with

$$k_e^2 = \frac{\omega^2 - k^2 v_{Ae}^2}{v_{Ae}^2}. \quad (21)$$

In addition, Y_m is the Bessel function of the second kind and of order m , and C_J and C_Y are two constants,

$$C_J = \frac{\pi a k_e}{2 k_i} [-k_i J_0(k_i a) Y_1(k_e a) + k_e J_1(k_i a) Y_0(k_e a)],$$

$$C_Y = \frac{\pi a k_e}{2 k_i} [-k_e J_1(k_i a) J_0(k_e a) + k_i J_0(k_i a) J_1(k_e a)]. \quad (22)$$

All other perturbations can be derived from Equation (15).

5. SOLUTION BY FOURIER INTEGRALS

5.1. Solution to Initial Value Problem

In this section we derive the expressions governing the propagation of an axisymmetric impulsive excitation such as that of Figure 1(b). The procedure to obtain the evolution of the perturbations after the magnetic tube suffers a localized transverse displacement is described in detail in Paper I, where all the relevant information can be found; here only the main equations are given. The initial value problem is specified by two initial conditions on the radial displacement,

$$\xi_r(t=0, r, z) = f(r, z),$$

$$\frac{\partial \xi_r}{\partial t}(t=0, r, z) = g(r, z). \quad (23)$$

To impose these initial conditions we write the Fourier transform of $\xi_r(t, r, z)$ with respect to z ,

$$\tilde{\xi}_r(t, r, k) = \int_{-\infty}^{\infty} \xi_r(t, r, z) e^{-ikz} dz. \quad (24)$$

For a given longitudinal wavenumber, $\tilde{\xi}_r(t, r, k)$ can be expressed as a linear combination of proper and improper eigenfunctions,

$$\tilde{\xi}_r(t, r, k) = \sum_{j=1}^N [A_j^+(k) e^{-i\omega_j(k)t} + A_j^-(k) e^{i\omega_j(k)t}] \hat{\xi}_j(r, k) + \int_{|k|v_{Ae}}^{\infty} [A_{\omega}^+(k) e^{-i\omega t} + A_{\omega}^-(k) e^{i\omega t}] \hat{\xi}_{\omega}(r, k) d\omega, \quad (25)$$

where $\omega_j(k) > 0$ and $\omega > 0$ are assumed with no loss of generality. In this expression, the fundamental fast sausage mode ($j = 1$) and its radial overtones ($j = 2, 3, \dots$) have frequencies $\pm\omega_j(k)$, which are the solutions to the dispersion relation (Equation (16)), and their radial displacement, $\hat{\xi}_j(r, k)$, is given by Equation (13). The contribution of each of these proper modes to Equation (25) depends on the amplitude $A_j^{\pm}(k)$, where the + and - signs correspond to propagation in opposite directions along the magnetic tube. Moreover, N is the number of proper sausage modes for the selected longitudinal wavenumber. For $|k| \leq k_{c1}$ no proper

eigenmodes exist and so $N = 0$, which means that the sum is not present in Equation (25); for $k_{c1} < |k| \leq k_{c2}$ only the fundamental fast sausage mode exists and then $N = 1$; and so on. Regarding improper modes, their contribution to Equation (25) has the form of an integral because they have a continuous variation of frequency for a given k . The improper modes eigenfunction $\hat{\xi}_{\omega}(r, k)$ has been presented in Equation (20).

We next define the Hilbert space of functions on the interval $[0, \infty)$ by the scalar product

$$\langle \eta, \zeta \rangle = \int_0^{\infty} \rho_0(r) (\eta \zeta^*) r dr. \quad (26)$$

With this definition, the eigenfunctions satisfy the orthogonality conditions

$$\langle \hat{\xi}_j, \hat{\xi}_l \rangle = 0 \quad (j \neq l),$$

$$\langle \hat{\xi}_j, \hat{\xi}_{\omega} \rangle = 0,$$

$$\langle \hat{\xi}_{\omega}, \hat{\xi}_{\omega'} \rangle = q(\omega) \delta(\omega - \omega'), \quad (27)$$

where $\omega, \omega' > 0$ and

$$q(\omega) = \frac{\rho_e a^4 v_{Ae}^2 k_e^2}{\omega} (C_J^2 + C_Y^2), \quad (28)$$

see Appendix B.

To determine the functions $A_j^{\pm}(k)$ ($j = 1, \dots, N$) and $A_{\omega}^{\pm}(k)$ we use the initial conditions. Taking $t = 0$ in Equation (25) we obtain

$$\tilde{f}(r, k) = \sum_{j=1}^N [A_j^+(k) + A_j^-(k)] \hat{\xi}_j(r, k) + \int_{|k|v_{Ae}}^{\infty} [A_{\omega}^+(k) + A_{\omega}^-(k)] \hat{\xi}_{\omega}(r, k) d\omega, \quad (29)$$

$\tilde{f}(r, k)$ being the Fourier transform with respect to z of $f(r, z)$. Now, differentiating Equation (25) with respect to t and substituting $t = 0$ yields

$$\tilde{g}(r, k) = -i \sum_{j=1}^N \omega_j(k) [A_j^+(k) - A_j^-(k)] \hat{\xi}_j(r, k) - i \int_{|k|v_{Ae}}^{\infty} \omega [A_{\omega}^+(k) - A_{\omega}^-(k)] \hat{\xi}_{\omega}(r, k) d\omega, \quad (30)$$

with $\tilde{g}(r, k)$ the Fourier transform of $g(r, z)$ with respect to z .

The next step is to take the scalar product of Equations (29) and (30) with $\hat{\xi}_j(r, k)$. Using Equation (27), this results in two algebraic expressions for $A_j^{\pm}(k)$ that lead to

$$A_j^{\pm}(k) = \frac{\mathcal{N}_j^{\pm}(k)}{2\omega_j(k) D_j(k)}, \quad (j = 1, 2, \dots, N), \quad (31)$$

with

$$\mathcal{N}_j^{\pm}(k) = -\frac{\rho_i K_0(\kappa_e a)}{k_i^2} \int_0^a [(\omega_j \tilde{f} \pm i \tilde{g}) k_i r J_1(k_i r)] dr + \frac{\rho_e J_0(k_i a)}{\kappa_e^2} \int_a^{\infty} [(\omega_j \tilde{f} \pm i \tilde{g}) \kappa_e r K_1(\kappa_e r)] dr, \quad (32)$$

$$D_j(k) = \frac{\rho_i K_0^2(\kappa_e a)}{k_i^4} \int_0^a (k_i r)^2 J_1^2(k_i r) \frac{dr}{r} + \frac{\rho_e J_0^2(k_i a)}{\kappa_e^4} \int_a^\infty (\kappa_e r)^2 K_1^2(\kappa_e r) \frac{dr}{r}. \quad (33)$$

Analytical expressions for the integrals in this formula can be obtained. Using Equation (14) and the relations (Abramowitz & Stegun 1964)

$$\begin{aligned} x J_1'(x) &= x J_0(x) - J_1(x), \\ x K_1'(x) &= -x K_0(x) - K_1(x), \end{aligned} \quad (34)$$

where a prime indicates a derivative, we obtain

$$\begin{aligned} \frac{d}{dx} \left\{ x^2 [J_0^2(x) + J_1^2(x)] \right\} &= 2x J_0^2(x), \\ \frac{d}{dx} \left\{ x^2 [K_0^2(x) - K_1^2(x)] \right\} &= 2x K_0^2(x). \end{aligned} \quad (35)$$

With the aid of these formulae we get

$$\int_0^a (k_i r)^2 J_1^2(k_i r) \frac{dr}{r} = \frac{k_i^2 a^2}{2} [J_0^2(k_i a) + J_1^2(k_i a)] - k_i a J_0(k_i a) J_1(k_i a), \quad (36)$$

$$\int_a^\infty (\kappa_e r)^2 K_1^2(\kappa_e r) \frac{dr}{r} = \frac{\kappa_e^2 a^2}{2} [K_0^2(\kappa_e a) - K_1^2(\kappa_e a)] + \kappa_e a K_0(\kappa_e a) K_1(\kappa_e a). \quad (37)$$

Inserting these expressions in Equation (33) $D_j(k)$ can be cast as

$$\begin{aligned} D_j(k) &= \frac{\rho_i K_0^2(\kappa_e a)}{k_i^4} \left\{ \frac{k_i^2 a^2}{2} [J_0^2(k_i a) + J_1^2(k_i a)] \right. \\ &\quad \left. - k_i a J_0(k_i a) J_1(k_i a) \right\} \\ &\quad + \frac{\rho_e J_0^2(k_i a)}{\kappa_e^4} \left\{ \frac{\kappa_e^2 a^2}{2} [K_0^2(\kappa_e a) - K_1^2(\kappa_e a)] \right. \\ &\quad \left. + \kappa_e a K_0(\kappa_e a) K_1(\kappa_e a) \right\}. \end{aligned} \quad (38)$$

Furthermore, the amplitudes of improper modes, $A_\omega^\pm(k)$, are obtained in a similar fashion by taking the scalar product of Equations (29) and (30) with $\tilde{\xi}_\omega(r, k)$. Then we have

$$A_\omega^\pm(k) = \frac{\mathcal{N}_\omega^\pm(k)}{2\omega q(\omega)}, \quad (39)$$

where

$$\begin{aligned} \mathcal{N}_\omega^\pm(k) &= -\frac{\rho_i a^2 k_e^2}{k_i^2} \int_0^a (\omega \tilde{f} \pm i \tilde{g}) k_i r J_1(k_i r) dr \\ &\quad - \rho_e a^2 \int_a^\infty (\omega \tilde{f} \pm i \tilde{g}) k_e r [C_J J_1(k_e r) \\ &\quad + C_Y Y_1(k_e r)] dr. \end{aligned} \quad (40)$$

We can finally present the main expression of this paper. The inverse Fourier transform of $\tilde{\xi}_r(t, r, k)$ with respect to k yields the radial displacement as a function of r and z ,

$$\xi_r(t, r, z) = \frac{1}{2\pi} \int_{-\infty}^{\infty} \tilde{\xi}_r(t, r, k) e^{ikz} dk, \quad (41)$$

where $\tilde{\xi}_r(t, r, k)$ is given in Equation (25). All other perturbations (i.e., magnetic field, velocity, and density) are described by analogous formulas.

5.2. Amplitudes for Specific Initial Conditions

The expressions presented in Section 5.1 are valid for any axisymmetric initial conditions described by the functions $f(r, z)$ and $g(r, z)$ in Equation (23). Here we consider $g(r, z) = 0$ (i.e., the perturbed system is initially at rest) and $f(r, z)$ given by

$$f(r, z) = \xi_0 \psi(r) \exp(-z^2/\Delta^2), \quad (42)$$

with

$$\psi(r) = \begin{cases} r/a, & r \leq a, \\ a/r, & r \geq a. \end{cases} \quad (43)$$

The parameter Δ determines the length of the initial tube disturbance. In addition, ξ_0 is the maximum radial displacement of the tube boundary at $t = 0$. In our calculations we consider various values of Δ .

The Fourier transforms of $f(r, z)$ and $g(r, z)$ with respect to z are

$$\begin{aligned} \tilde{f}(r, k) &= \xi_0 \sqrt{\pi} \Delta \psi(r) \exp(-\Delta^2 k^2/4), \\ \tilde{g}(r, k) &= 0, \end{aligned} \quad (44)$$

and so the following formulae for $\mathcal{N}_j^\pm(k)$ and $\mathcal{N}_\omega^\pm(k)$ can be derived

$$\begin{aligned} \mathcal{N}_j^\pm(k) &= -a \xi_0 \sqrt{\pi} \Delta \omega_j \exp(-\Delta^2 k^2/4) K_0(\kappa_e a) \\ &\quad \times \left\{ \frac{\rho_i J_2(k_i a)}{k_i^2} - \frac{\rho_e J_0(k_i a)}{\kappa_e^2} \right\}, \end{aligned} \quad (45)$$

$$\begin{aligned} \mathcal{N}_\omega^\pm(k) &= -a^3 \xi_0 \sqrt{\pi} \Delta \omega \exp(-\Delta^2 k^2/4) \left\{ \frac{\rho_i k_e^2}{k_i^2} J_2(k_i a) \right. \\ &\quad \left. + \rho_e [C_J J_0(k_e a) + C_Y Y_0(k_e a)] \right\}. \end{aligned} \quad (46)$$

Therefore, analytical expressions for all the integrals in the amplitudes $A_j^\pm(k)$ and $A_\omega^\pm(k)$ have been obtained. Note that if $g(r, z) = 0$ then $A_j^+(k) = A_j^-(k)$ and $A_\omega^+(k) = A_\omega^-(k)$.

The function $\psi(r)$ gives the radial distribution of ξ_r at $t = 0$. Inside the tube, this radial distribution must be different for axisymmetric and transverse perturbations: in this work it is given by r/a whereas in Paper I it is equal to 1. On the other hand, there is no a priori information about the variation of $\psi(r)$ outside the tube, other than its presumed decrease away from the magnetic tube. In Paper I this radial decrease is of the form $\exp(-(r^2 - a^2)/l^2)$, but here we prefer to choose $\psi(r) = a/r$ because this leads to a much better accuracy in the computation of the improper modes contribution. In order to make a comparison with the results of Paper I, the proper and improper mode amplitudes of transverse disturbances are presented in Appendix C for $\psi(r) = a/r$ outside the cylinder.

6. RESULTS

The procedure to obtain the perturbations with the help of Equations (25) and (41) is described in Section 5.4 of Paper I and thus is not repeated here. In this work we concentrate on

the radial displacement at a point on the magnetic tube boundary ($r = a$). The dimensionless results only depend on two parameters, namely the density ratio ρ_i/ρ_e (or equivalently the Alfvén speed ratio v_{Ai}/v_{Ae}) and Δ . This parameter determines the length of the initial perturbation, which is of the order of 4Δ ; see Equation (42). We use the parameter values $\rho_i/\rho_e = 4, 9$ and $\Delta = a, 2a$. If dimensional results are needed, then two more parameters are required: the tube radius, a , and Alfvén speed, v_{Ai} .

6.1. Contribution of Proper and Improper Modes

We first consider the radial displacement at the magnetic tube boundary for $t = 0$. This is obtained from Equations (41) and (25), where the contributions of proper and improper modes are computed separately. The black line in Figure 3 shows that this numerically computed ξ_r reproduces the Gaussian initial condition of Equations (23) and (42). In addition, Figure 3 also reveals that improper modes (red line) have a large contribution to the initial wave form. For the considered parameter values, this contribution is larger than that of proper modes (green line). The reason for the large amplitude of improper modes can be found in the wavenumber cut off of the fundamental fast sausage eigenmode, that does not exist for $|k| \leq k_{c1}$. Its overtones have even larger wavenumber cut offs. Then, given the initial disturbance of Equation (42) and its Fourier transform of Equation (44), that peaks at $k = 0$, the contributions to $\tilde{f}(r, k)$ for $|k| \leq k_{c1}$ cannot be accounted for by proper modes. This implies that improper modes must have an important contribution to the initial amplitude of the perturbation and, therefore, to the posterior evolution of the wave train propagation. Another significant feature of Figure 3 is that the contribution of both proper and improper modes extends well beyond the length of the tube affected by the initial disturbance. The two contributions display spatial variations that added together yield the Gaussian shape of Equation (44).

It is worth noting that improper eigenmodes are more relevant for the present axisymmetric disturbance than for the transverse disturbance: compare Figures 3 and 4(a) and (b) of Paper I. The main difference between fast kink and sausage proper modes is that the fundamental proper kink mode exists for all wavenumbers, so that it can account for the main part of the function $\tilde{f}(r, k)$. This fact lowers the importance of improper modes in the case of a transverse disturbance and also has a second effect: contrary to the case studied here, at $t = 0$ proper and improper modes are confined to the vicinity of the initial perturbation, such as revealed by Figures 4(a) and (b) of Paper I.

From Figure 3 we also see that the contribution of improper modes increases when either Δ is increased or ρ_i/ρ_e is decreased. We next explain this behavior. An increase of Δ corresponds to a longer initial perturbation, whose Fourier transform becomes more concentrated around $k = 0$. Since the fundamental fast sausage mode only exists for $|k| > k_{c1}$, an increase in Δ results in a decrease of $\tilde{f}(r, k)$ for $|k| > k_{c1}$, so that the contribution of proper modes becomes smaller. This is corroborated by Figures 4(a) and (b), where the contribution of proper modes to the amplitude of $\tilde{\xi}_r$ at $r = a$ is shown for two values of Δ . In addition, the role of the density ratio is to modify the cut off wavenumbers, in such a way that a decrease in ρ_i/ρ_e leads to a larger wavenumber cut off (see Figure 2).

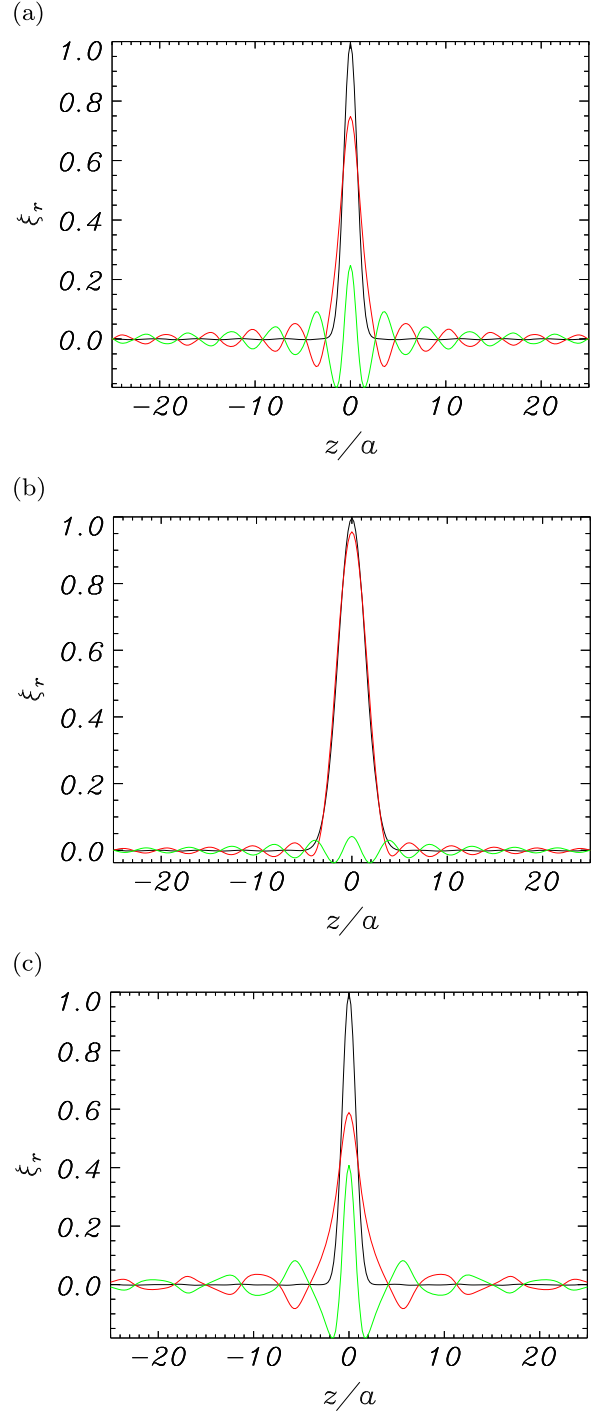


Figure 3. Initial shape of the magnetic tube boundary, given by Equations (42) and (43) with $r = a$. The radial displacement of the tube boundary is plotted at $t = 0$ as a function of the distance along the magnetic tube (black line). The contributions of proper and improper modes are shown as green and red lines, respectively. (a) Density ratio $\rho_i/\rho_e = 4$ and $\Delta = a$; (b) $\rho_i/\rho_e = 4$ and $\Delta = 2a$; (c) $\rho_i/\rho_e = 9$ and $\Delta = a$. According to Equation (42) the length of the initial disturbance is of the order of 4Δ .

This then yields a smaller contribution of proper modes: compare Figures 4(a) and (c).

Figure 4 also provides information about the relative importance of proper mode overtones. Such as expected, the largest amplitude of all proper modes corresponds to the fundamental fast sausage mode, whereas its radial overtones

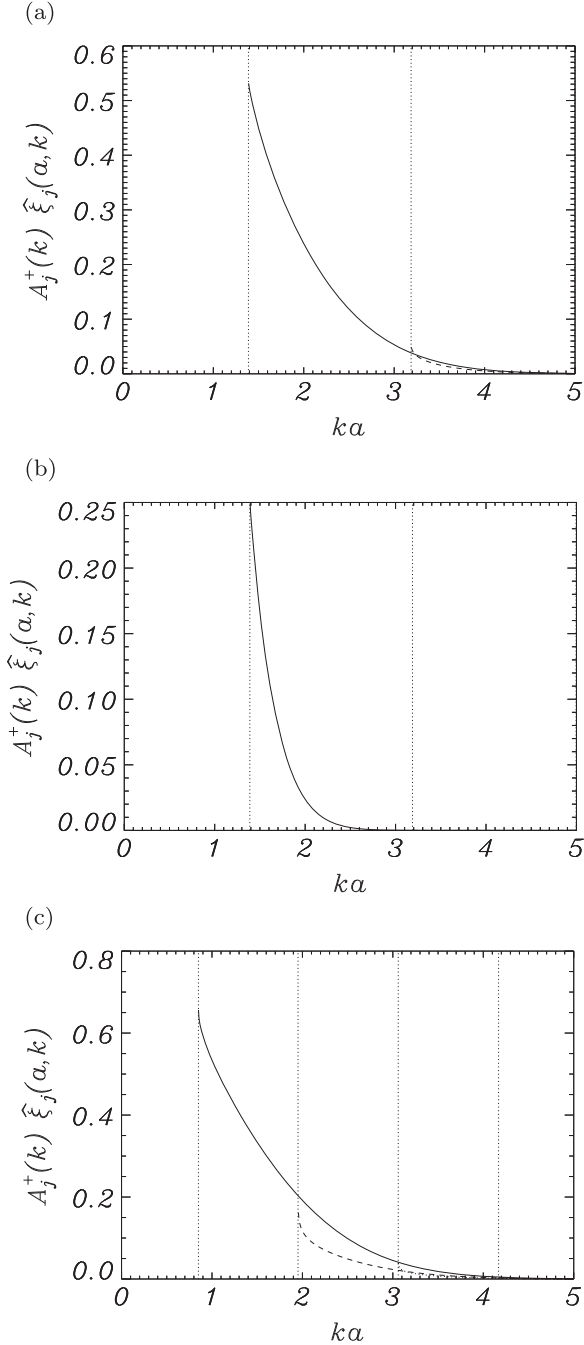


Figure 4. Proper mode contribution to the radial displacement as a function of the longitudinal wavenumber. When inserted in Equation (25), the product $A_j^+(k)\hat{\xi}_j(a, k)$ determines the contribution of each proper mode to the radial displacement for a fixed k . (a) $\rho_i/\rho_e = 4$ and $\Delta = a$; (b) $\rho_i/\rho_e = 4$ and $\Delta = 2a$; (c) $\rho_i/\rho_e = 9$ and $\Delta = a$. Solid, dashed, and dotted lines correspond to the fundamental mode and its first two overtones. The vertical dotted lines mark the wavenumber cut offs.

possess smaller amplitudes. By comparing panels (a) and (b) we see that longer initial perturbations result in a negligible amplitude of all radial overtones. We must mention that in Figures 4(a) and (b) only the fundamental mode and its first overtone are present (solid and dashed lines), although in panel (b) the first overtone has negligible amplitude, so its curve is invisible. Furthermore, in Figure 4(c) the dashed and dotted curves overlap for $3 \lesssim ka \lesssim 4$ and may seem to be just one.

6.2. Propagation of Wave Trains

6.2.1. Dispersive Behavior

Next, we concentrate on the evolution of the pulse in Figure 3(a). This initial perturbation splits in two identical wave trains that propagate symmetrically in both directions along the magnetic tube. The early stages of the propagating wave trains are presented in the animation of Figure 5. Figures 5(a)–(c) correspond to the separation of the two wave trains, whereas in Figure 5(d) these two features are fully formed. The strong dispersion of the axisymmetric perturbation can be well appreciated in this last panel: both wave packets have developed some 6 maxima and minima and their length is more than 4 times that of the perturbation at $t = 0$. Proper and improper modes contribute with similar amplitudes to the total signal represented in the animation of Figure 5. A secondary effect of wave dispersion is the strong reduction of the wave packet amplitude. In the absence of dispersion, the two wave packets in Figure 5(d) would have amplitude 0.5, whereas their actual peak-to-peak amplitude is under 0.3.

When discussing Figure 3 we explained that, when considered separately, the contributions of proper and improper modes affect a section of the magnetic tube much longer than that of the initial perturbation. At $t = 0$ these two contributions simply cancel out in the parts of the magnetic tube where the initial excitation is negligible. This situation also takes place for $t > 0$: although proper and improper mode contributions disturb a large part of the magnetic tube, their sum is concentrated in a smaller section. Thus, ahead of the propagating wave fronts, where the initial perturbation has not yet arrived, these contributions are spatially out of phase and cancel out. This is also found at $-2 \lesssim z/a \lesssim 2$ in Figure 5(d) because the two wave packets have moved beyond this section of the magnetic tube, which is barely disturbed.

The green and red curves in Figure 5 reveal the separate behavior of proper and improper modes. The first ones propagate with group velocity ranging from $\sim 0.84v_{Ai}$ (see the minimum of the black line in Figure 2(c)) to $v_{Ae} = 2v_{Ai}$. Because of this variation of group velocity the green curve displays some dispersion, that becomes more clear for later times (this issue will be discussed below with the help of Figure 6). On the other hand, improper modes propagate at their own phase speed and so are subject to phase mixing, that leads to stronger dispersion. This dispersive behavior in turn causes a severe amplitude decrease that is clearly visible when comparing the red lines in Figures 5(a) and (d). The asymptotic behavior of improper modes for large t was studied in Section 5.3 of Paper I, that deals with a transverse initial perturbation. It was found that the contribution of improper modes decays as $1/t$. The same applies to the present axisymmetric perturbation.

At $t = 20\tau_{Ai}$ the perturbation of Figure 3(a), whose early development is presented in Figure 5, is spread over a long section of the tube of length $\sim 30a$ (compare this value with the initial length of the perturbation $\sim 4a$); see Figure 6(a). Here the total perturbation of the radial displacement and the contributions of proper and improper modes are represented with the usual colors (black, green, and red, respectively). The vertical lines denote the position of a point initially at $z = 0$ and moving at specific velocities: the dash-dotted, dashed, and dotted lines correspond to the maximum group velocity of proper modes ($2v_{Ai}$), the minimum group velocity of the

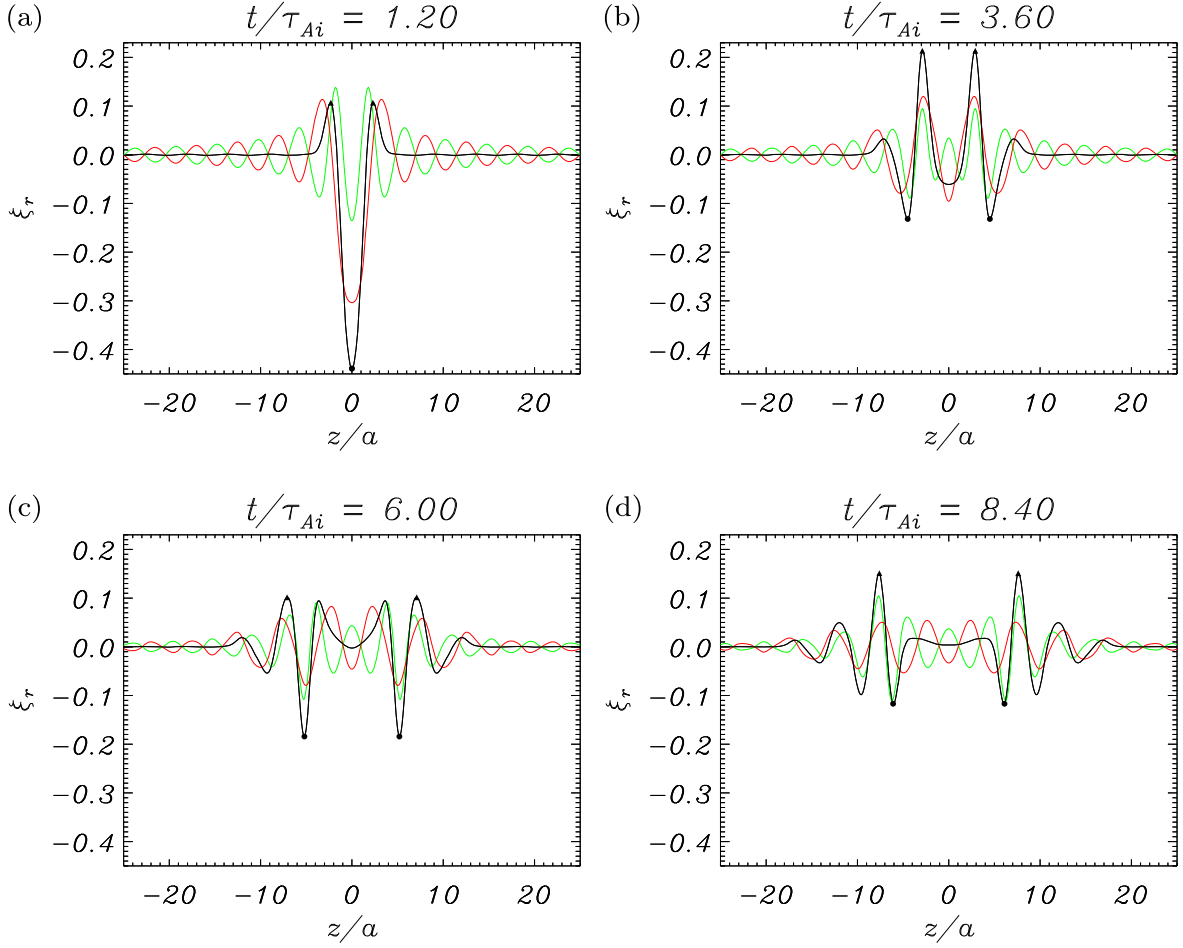


Figure 5. Shape of the magnetic tube boundary for several times (shown at the top of each frame). The radial displacement at $r = a$ is plotted as a function of z . This figure shows the early evolution of the initial pulse of Figure 3(a). Black lines correspond to ξ_r , while green and red lines correspond to the contributions of proper and improper modes, respectively. The density ratio is $\rho_i/\rho_e = 4$ and the length of the initial disturbance is of the order of $4a$. (Triangles and squares mark the maximum and minimum values of ξ_r .)

(An animation of this figure is available.)

fundamental fast sausage mode ($0.84v_{Ai}$), and the minimum group velocity of its first overtone ($0.73v_{Ai}$). This range of group velocities determines the length of the wave train at a given time. The wave train shape is controlled by two more features: the dependence $c_g(k)$ of proper modes (black lines in Figure 2(c)) and the amplitude of the perturbation (Figure 4(a)). Wavenumbers slightly above the cut off occupy the leading part of the wave packet and have the largest amplitudes, but their c_g varies strongly with k . Thus, these wavenumbers are strongly dispersed and contribute moderately to the wave train amplitude. On the other hand, wavenumbers $ka \gtrsim 1.6$ have group velocities in a small range around the minimum of c_g and for this reason the maximum amplitude of the wave train is found near the dashed line in Figure 6(a). A side effect of the wave dispersion is the decrease of the wave packet amplitude (compare Figures 5(d) and 6(a)). Again, note the cancellation of proper and improper mode contributions ahead and behind the propagating wave train.

6.2.2. Influence of the Initial Perturbation Length and the Density Contrast on the Wave Train Dispersion

If the internal to external density ratio is kept fixed and the length of the initial disturbance is doubled (Figure 6(b)) the

dispersion of the wave train in its constituent frequencies does not change because the group velocity of proper modes is the same. Then, the positions of maxima and minima in Figures 6(a) and (b) are the same. Nevertheless, according to Figures 3(a) and (b) and 4(a) and (b), a longer initial disturbance corresponds to smaller amplitudes of proper modes and for this reason the amplitude of the wave train is much smaller for $\Delta = 2a$ than for $\Delta = a$.

Finally, we consider the case of a magnetic tube with a larger internal to external density contrast ($\rho_i/\rho_e = 9$; Figure 6(c)). In this case the minimum group velocity of the fundamental fast sausage mode and its first overtone are similar to those for $\rho_i/\rho_e = 4$ and this implies that the position of the vertical dashed and dotted lines in Figures 6(a) and (c) are similar. But by increasing the density ratio from 4 to 9, the maximum group velocity of proper modes increases from $2v_{Ai}$ to $3v_{Ai}$ and so the front of the wave train travels considerably faster. Hence, the wave packet extends over a much longer section of the magnetic tube, with length $\sim 50a$. The leading part of the wave train has a small amplitude because of the strong gradient of $c_g(k)$ near the cut-off wavenumber. In addition, the largest amplitude is found at the back of the wave packet, where, again, a wide range of wavenumbers with values of c_g near the minimum group velocity concentrate their contribution.

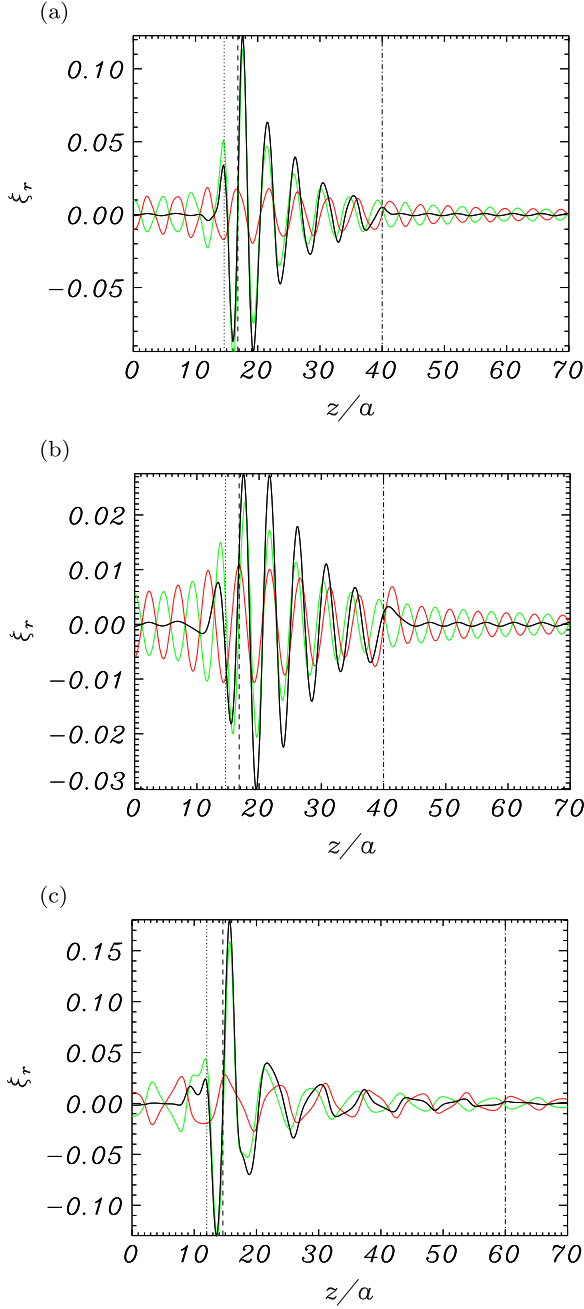


Figure 6. Shape of the magnetic tube boundary at $t = 20\tau_{Ai}$. The three panels correspond to the wave trains caused by the initial disturbances of Figure 3, with the same meaning of line colors. The vertical lines give the position of a point initially at $z = 0$ and traveling at a constant speed equal to the maximum group velocity of proper modes (dash-dotted line), the minimum group velocity of the fundamental proper mode (dashed line), and the minimum group velocity of the first proper mode overtone (dotted line).

6.2.3. Wave Train Position and Maximum Amplitude

The wave train propagation speed and amplitude are next quantified. We consider the evolution of the propagating wave packet (e.g., as in Figure 5 and the associated animation) and for each time keep the position, z_m , where the absolute value of the radial displacement, $|\xi_r|$, is maximum. The solid lines in Figure 7(a) present the temporal variation of z_m for the parameter values used above. We see that in the three cases the propagation speed is roughly constant and in the range $0.75-1v_{Ai}$. The saw-toothed shape of these curves is caused

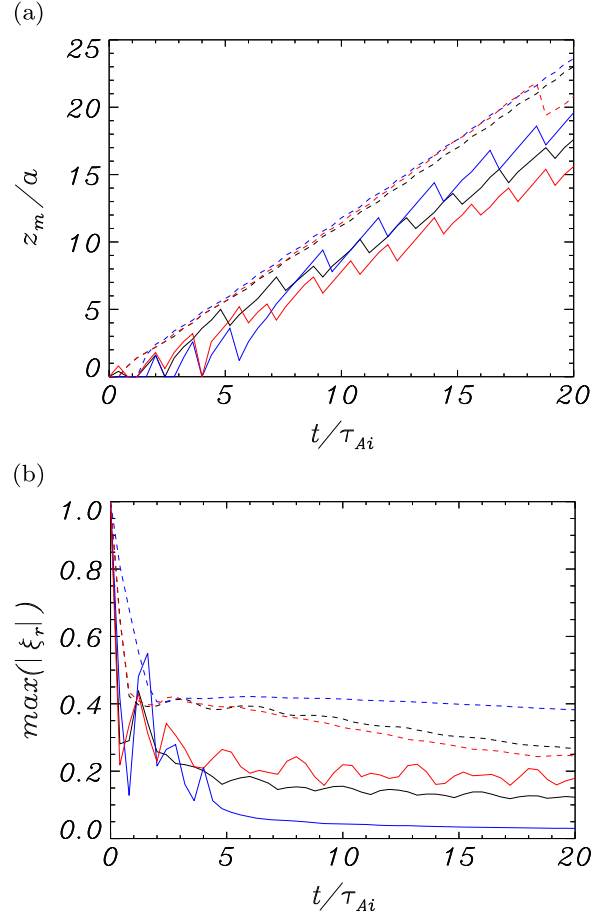


Figure 7. Time variation of (a) the position along the magnetic tube where the radial displacement attains its maximum unsigned value; (b) the maximum unsigned value of the radial displacement. The line colors correspond to $\rho_i/\rho_e = 4$, $\Delta = a$ (black), $\rho_i/\rho_e = 4$, $\Delta = 2a$ (blue), and $\rho_i/\rho_e = 9$, $\Delta = a$ (red). Solid and dashed lines correspond to axisymmetric and transverse initial excitations, respectively.

by dispersion, which makes the extremum of ξ_r to alternate between positive and negative sign; see the animation associated with Figure 5 for $t/\tau_{Ai} \sim 4.9$ or $t/\tau_{Ai} \sim 7$, for example.

Figure 7(b) provides a clear description of the wave train amplitude decrease produced by the joint effect of wave emission by leakage (discussed in Section 6.4) and dispersion. The blue line confirms that longer perturbations undergo much stronger attenuation than shorter ones, such as explained before. In addition, smaller density contrasts also lead to slightly stronger attenuation: compare the black and red curves. The irregular behavior found in Figure 7(b) has a common origin with the saw-toothed shape of panel (a).

6.3. Comparison of Signals Caused by Axisymmetric and Transverse Disturbances

Here we compare the response of the magnetic tube boundary under initial axisymmetric and transverse disturbances, respectively described in this paper and in Paper I. To make this comparison we consider the wave train passage at a fixed position ($z = 20a$) and plot the radial displacement as a function of time (see Figure 8, in which the left and right columns correspond to axisymmetric and transverse disturbances).

Inspection of Figure 8 reveals the very different dispersive properties of fast sausage and kink waves. The first ones

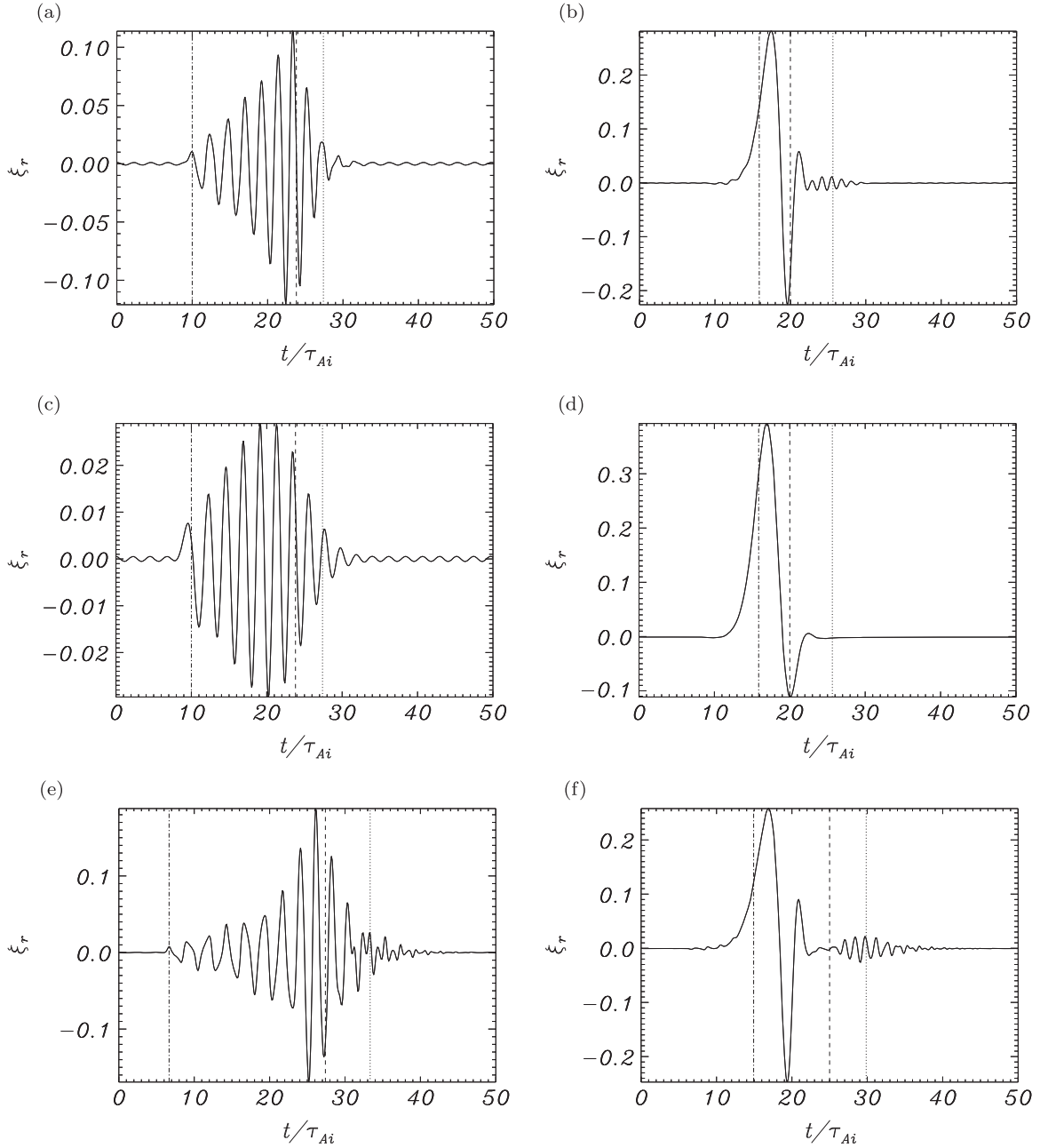


Figure 8. Radial displacement of the magnetic tube boundary at a distance $z = 20a$ from the initial perturbation. Left column: axisymmetric (sausage) perturbation; right column: transverse (kink) perturbation. (a) and (b) $\rho_i/\rho_e = 4$, $\Delta = a$; (c) and (d) $\rho_i/\rho_e = 4$, $\Delta = 2a$; (e) and (f) $\rho_i/\rho_e = 9$, $\Delta = a$. The vertical lines have the same meaning as in Figure 6.

display rapid oscillations with period $\sim 3\tau_{Ai}$, whereas the latter have only one full oscillation with larger amplitude and period $\sim 6\tau_{Ai}$. The Alfvén transit time in coronal loops, τ_{Ai} , is of the order of 1 s. This disparate behavior occurs because the fundamental fast kink mode does not have a cut-off wavenumber and its group velocity has a more moderate range of variation than that of its sausage counterpart. The length of the initial perturbation plays a different role in the propagation of axisymmetric and transverse disturbances. In the first case (compare Figures 8(a) and (c)) a longer disturbance imparts less energy to proper modes and the wave train disperses more quickly, with a stronger decrease of its amplitude. On the other hand, a longer transverse disturbance (compare Figures 8(b) and (d)) imparts less energy to the first overtone (and so the

trailing oscillations are missing in panel (d)) and the fundamental mode receives more energy in the long-wavelength regime, for which c_g has a small spread. This then results in less dispersion of the wave train. These results are in agreement with Figure 7(b): the longest axisymmetric perturbation (solid blue line) displays the highest damping, while the opposite happens with transverse perturbations (see dashed lines).

Regarding the propagation speed of the wave packets, transverse disturbances travel at a speed $\sim 1.2v_{Ai}$ that is independent of the density contrast and the length of the initial excitation (Figure 7(a)). Transverse disturbances then travel somewhat faster than axisymmetric ones.

It is also worth noting that the first fast kink mode overtone leaves its imprint in Figures 8(b) and (f) as small amplitude, short period oscillations that arrive at the detection point after the main pulse. Finally, the small amplitude oscillations in panels (a) and (c) before and after the wave train passage are numerical artifacts.

6.4. Wave Leakage

The improper modes are closely related to leaky quasi-modes studied by, e.g., Cally (1986, 2003); see also the discussion by Andries & Goossens (2007). The interference of improper modes will create a wave front propagating from the tube in the radial direction. The leaky quasi-modes describe the so-called intermediate asymptotic of this wave front (see Ruderman & Roberts 2006, for a discussion of the role of leaky quasi-modes in the case of kink waves).

Wave radiation after the initial excitation can be well appreciated by plotting snapshots of the dependence of ξ_r with respect to r for several times (Figure 9). Panel (a) shows the imposed radial profile of the radial displacement at $t = 0$, given by Equation (43), with improper modes (red curve) having a more important contribution than proper modes (green curve). The subsequent temporal evolution of ξ_r shows oscillations inside the magnetic cylinder ($0 \leq r/a \leq 1$) and in its vicinity, together with a wave pulse propagating outwards in the radial direction, that is specially visible in panel (d) as a depression in ξ_r in the range $3 \lesssim r/a \lesssim 7$. This propagating feature is clearly caused by improper modes because the amplitude of proper modes at its position is negligible.

The wave emission process has been presented here by doing the cuts of Figure 9 at the center of the initial perturbation ($z = 0$), but as far as the amplitude of improper modes is non zero, it also takes place at other positions along the magnetic tube when they are affected by the propagating disturbance.

7. DISCUSSION

In this paper we have used a method based on Fourier integrals to solve the initial value problem of impulsively excited axisymmetric (i.e., sausage) perturbations in a uniform, dense, cylindrical magnetic tube. The linear and $\beta = 0$ approximations have been assumed. This method gives analytical expressions for the perturbations (plasma displacement, density, velocity, and magnetic field) that require the numerical computation of the two integrals in Equations (25) and (41). The accuracy of the results depends exclusively on the precision of the numerical computation of these integrals. An advantage of this method is that one can select which perturbations will be computed and at which spatial position(s) and time(s).

The present initial value problem requires initial conditions on the radial displacement and its time derivative. The first of these conditions is given by Equations (42) and (43), in which we have assumed that the radial variation of ξ_r is equal to a/r outside the magnetic cylinder. Such as mentioned above, this radial profile differs from that assumed in Paper I and here there is room to some arbitrariness since we have no knowledge on the radial variation of actual impulsive perturbations in the Sun's atmosphere. It is probably worth considering different external profiles of $\psi(r)$, e.g., Gaussian, inversely proportional to r , exponentially decreasing, and studying their effect on the dispersion of wave trains, both axisymmetric and transverse.

The impulsive generation of fast sausage wave trains in a dense magnetic tube has also been studied before by numerically solving the linearized MHD equations. Most of these works use a Cartesian slab to represent the magnetic tube (Murawski & Roberts 1993a, 1993b; Nakariakov et al. 2004, 2005, 2012; Jelínek and Karlický 2010; Mészáros et al. 2014). In the solar context, only Selwa et al. (2004) have considered this problem in cylindrical geometry, although they did not take into account the dispersive behavior of the propagating wave packet.

One of the key features of the present paper is the importance of the group velocity in the dispersion of a concentrated perturbation. Concerning fast sausage wave trains, this was already acknowledged by Roberts et al. (1984) and later by other authors (e.g., Nakariakov & Roberts 1995; Nakariakov et al. 2004). In addition to this, we have emphasized the role of the length of the initial perturbation and the internal to external density ratio in the wave packet dispersion (Figures 6 and 8). We have found that longer initial perturbations have much lower amplitudes because the initial excitation imparts less energy to proper modes (Figure 7(b)). In addition, larger values of the density ratio lead to a wider wave packet that nevertheless has a larger amplitude because most of the oscillatory energy is concentrated in its trailing part. Some of these results have also been found in a non-uniform dense slab by Nakariakov et al. (2005).

We are now concerned with the observational implications of our work. Fast magnetosonic waves can, potentially, be used as a diagnostic tool. Using the observation of the dispersive spreading of a fast sausage wave packet it is possible to estimate the transversal size of the wave guide. Thus an estimate complementary to one found in the direct observation can be obtained. In addition, one of the main conclusions of Paper I is that a spatially concentrated, transverse disturbance of a magnetic tube gives rise to non-negligible density perturbations that take their maximum value at the tube boundary. The reason for these density perturbations is that fast kink waves are compressive for longitudinal wavelengths of the order of the tube radius. The axisymmetric wave trains studied in the present work also generate density perturbations caused by the compressive character of fast sausage waves. Both transverse and axisymmetric pulses cause short period oscillations (of the order of seconds in coronal loops). To determine whether the wave trains propagating along coronal loops studied by Williams et al. (2001, 2002), Katsiyannis et al. (2003; and similar events detected in solar radio bursts, see Mészáros et al. 2009, 2011; Karlický et al. 2013) are caused by fast sausage or kink excitations it is necessary to carry out a forward modeling of the MHD perturbations to determine how they would appear when observed with available instruments. Cooper et al. (2003a, 2003b) assumed that the observed emission intensity in optically thin coronal lines is proportional to the line integral along the line of sight (LOS) of the electron number density squared. They considered fast sausage and kink waves with fixed wavelength and different orientations of the magnetic tube axis with respect to the LOS. They concluded that the two wave modes generate similar amplitudes of integrated density variations. Nevertheless, the integrated intensity alone does not govern the line intensity and formation of emission lines. De Moortel & Bradshaw (2008) took into account that it is actually governed by a complex, nonlinear interaction between the density squared, the ionization balance

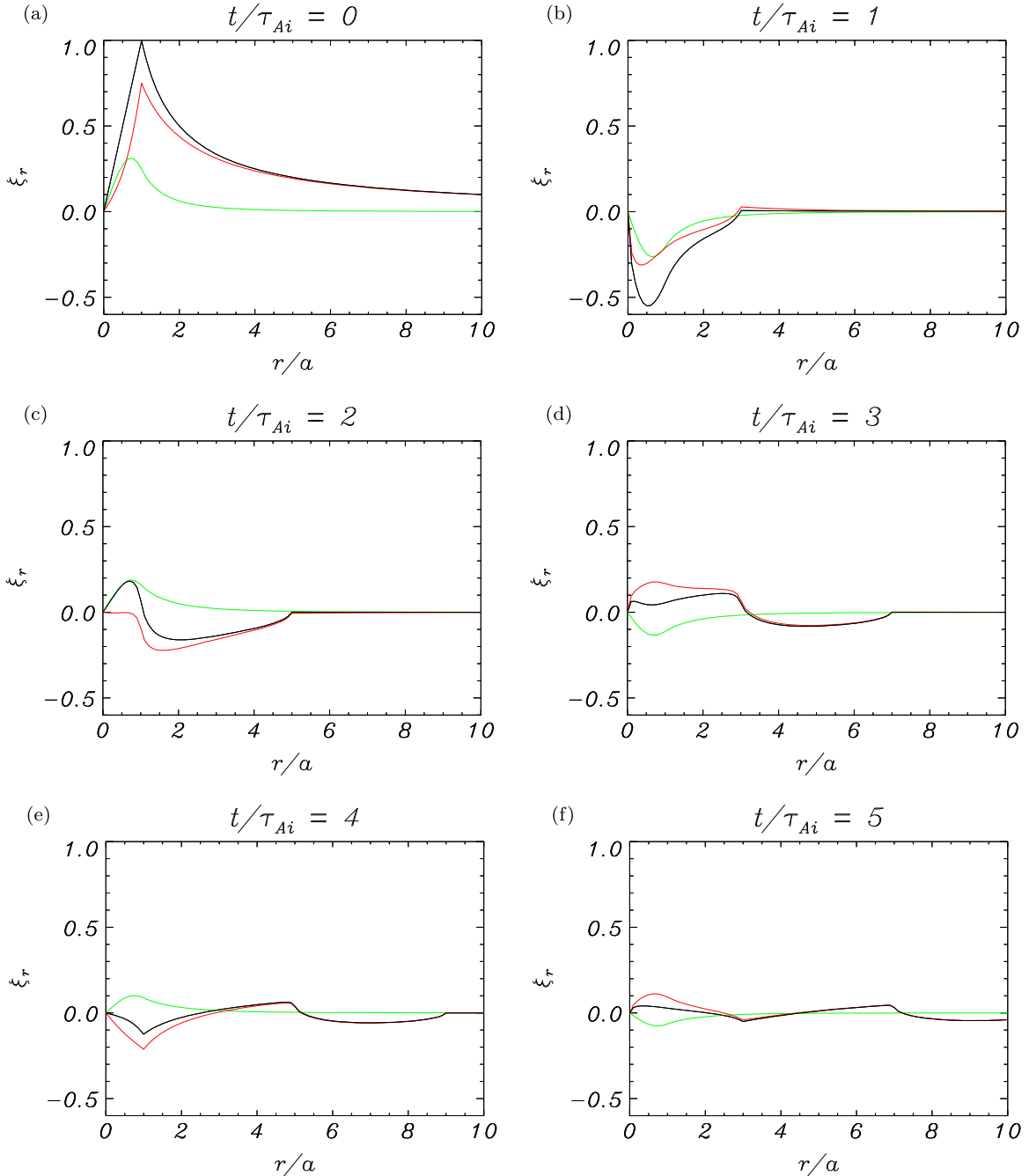


Figure 9. Radial displacement of the plasma as a function of radial distance at $z = 0$ and for different times, shown above each frame. Black lines correspond to the displacement ξ_r , while green and red lines correspond to the contributions of proper and improper modes, respectively. The density ratio is $\rho_i/\rho_e = 4$ and the length of the initial disturbance is of the order of $4a$.

and emissivity, and the instrument response function. The important point here is that the ionization equilibrium timescale of Fe x and Fe xii ions in a coronal environment is of the order of a few to tens of seconds. The effect of the ionization balance can be ignored only if the wave period is much longer than this timescale. Otherwise, observed intensity perturbations do not necessarily behave like the theoretical temperature and density. Therefore, to make a theoretical interpretation of the ~ 6 s oscillations described by Williams et al. (2001, 2002), Katsiyannis et al. (2003) a careful forward modeling of impulsively excited fast sausage and kink perturbations is required. Antolin & van Doorselaere (2013; see also

Reznikova et al. 2014) studied the influence of LOS angle and spatial, temporal, and spectral resolution of observing instruments on fast sausage wave observables. Under the assumption of equilibrium ionization, these authors concluded that the intensity variation can be very low ($\lesssim 4\%$ for Fe ix 171 Å) or significant ($\lesssim 35\%$ for Fe xii 193 Å). Most of the intensity variation, however, disappears when considering the radiative relaxation times of the ions. Another important conclusion of this work is that the intensity modulation has strong dependence on the LOS angle and on the spatial and temporal resolutions. Our future aim is to repeat the

calculations of Antolin & van Doorselaere (2013) for impulsive initial excitations of the fast sausage and kink types.

Fast sausage waves are very good candidates for coronal plasma heating due to their leaky nature. In the presence of dissipative effects the energy of trapped waves is mainly dissipated near wave guides, i.e., magnetic tubes, while a substantial part of the leaky wave energy is spread in the surrounding plasma in the form of fast magnetosonic waves. This wave leakage is caused by the interference of improper modes, that causes a wave front propagating away from the tube (Figure 9). These emitted waves can be readily damped by various mechanisms.

J. T. acknowledges support from the Spanish Ministerio de Educación y Ciencia through a Ramón y Cajal grant. R. O. and J. T. also acknowledge the funding provided under the project AYA2011-22846 by the Spanish MICINN and FEDER Funds. R. O. is indebted to D. W. Fanning for making available the Coyote Library of IDL programs (<http://www.idlcoyote.com/>) and to W. Rosenheinrich for his table of Bessel functions integrals (<http://www.fh-jena.de/~rsh/Forschung/Stoer/besint.pdf>). M. S. R. also acknowledges the support by the STFC grant. We are grateful to the anonymous referee for useful suggestions that helped improve the paper and to M. Carbonell for his comments on the manuscript.

APPENDIX A

FREQUENCY OF PROPER MODES FOR LARGE k

Our purpose here is to study the solutions to the dispersion relation

$$\frac{J_1(k_i a)}{k_i a J_0(k_i a)} + \frac{K_1(\kappa_e a)}{\kappa_e a K_0(\kappa_e a)} = 0 \quad (47)$$

in the limit of very large longitudinal wavenumber, i.e., for $ka \gg 1$. We make use of the asymptotic formulae for large arguments (Abramowitz & Stegun 1964)

$$K_0(x) \sim K_1(x) \sim \sqrt{\frac{\pi}{2x}} e^{-x}. \quad (48)$$

Figure 2 shows that, for $ka \gg 1$, ω/k is not close to v_{Ai} and so $\kappa_e a \gg 1$. Then, the second term in the dispersion relation is

$$\frac{K_1(\kappa_e a)}{\kappa_e a K_0(\kappa_e a)} \approx \frac{1}{\kappa_e a} \ll 1. \quad (49)$$

Again using Figure 2 we see that, for $ka \gg 1$, ω/k is close to v_{Ai} and so k_i is not large. Since the second term in Equation (47) is small, the first one also has to be small. This is only possible when $k_i a$ is close to one of the zeros of the function $J_1(x)$, which are j_{1j} , $j = 1, 2, \dots$. As a result, we have

$$\omega^2 = k^2 v_{Ai}^2 \left(1 + \frac{\rho_i j_{1j}^2}{\rho_e k^2 a^2} \right). \quad (50)$$

From this expression, the phase speed and group velocity for large longitudinal wavenumber are

$$\begin{aligned} c_{ph} &\approx v_{Ai} \left(1 + \frac{\rho_i j_{1j}^2}{2\rho_e k^2 a^2} \right), \\ c_g &\approx v_{Ai} \left(1 - \frac{\rho_i j_{1j}^2}{2\rho_e k^2 a^2} \right). \end{aligned} \quad (51)$$

We conclude that as ka tends to infinity, c_{ph} tends to v_{Ai} from above and c_g tends to v_{Ai} from below.

APPENDIX B

CALCULATION OF $q(\omega)$

Using Equation (20) we write the expression for the scalar product of two improper eigenfunctions as

$$\begin{aligned} \langle \hat{\xi}_\omega, \hat{\xi}_{\omega'} \rangle &= \frac{\rho_i a^4 k_e^2 k_e'^2}{k_i k_i'} \int_0^a J_1(k_i r) J_1(k_i' r) r dr \\ &+ \rho_e a^4 k_e k_e' \int_a^\infty F_1(k_e r) F_1(k_e' r) r dr, \end{aligned} \quad (52)$$

where

$$F_1(x) = C_J J_1(x) + C_Y Y_1(x). \quad (53)$$

Now we use the formulae

$$\begin{aligned} J_1(z) &= \sqrt{\frac{2}{\pi z}} \cos\left(z - \frac{3}{4}\pi\right) [1 + j_1(z)], \\ Y_1(z) &= \sqrt{\frac{2}{\pi z}} \sin\left(z - \frac{3}{4}\pi\right) [1 + y_1(z)], \end{aligned} \quad (54)$$

where $j_1(z)$ and $y_1(z)$ decay as z^{-1} when $z \rightarrow \infty$. Using these formulae, after some algebra, we rewrite Equation (52) as

$$\langle \hat{\xi}_\omega, \hat{\xi}_{\omega'} \rangle = \Gamma(\omega, \omega') + \Upsilon(\omega, \omega'), \quad (55)$$

where

$$\Gamma(\omega, \omega') = \Gamma_1(\omega, \omega') + \Gamma_2(\omega, \omega') + \Gamma_3(\omega, \omega'), \quad (56)$$

$$\Gamma_1(\omega, \omega') = \frac{\rho_i a^4 k_e^2 k_e'^2}{k_i k_i'} \int_0^a J_1(k_i r) J_1(k_i' r) r dr, \quad (57)$$

$$\begin{aligned} \Gamma_2(\omega, \omega') &= \frac{\rho_e a^4 \sqrt{k_e k_e'}}{\pi} \\ &\times \int_a^\infty \left\{ [C_J C_J' j_1(k_e' r) + C_J C_Y' y_1(k_e' r)] \right. \\ &\times \cos\left(k_e r - \frac{3}{4}\pi\right) \\ &\left. + [C_Y C_J' j_1(k_e' r) + C_Y C_Y' y_1(k_e' r)] \right\} \end{aligned}$$

$$\begin{aligned}
& \times \sin \left(k_e r - \frac{3}{4}\pi \right) \\
& + [C_J C'_{J1}(k_e r) + C_Y C'_{Y1}(k_e r)] \\
& \times \cos \left(k'_e r - \frac{3}{4}\pi \right) \\
& + [C_J C'_{Y1}(k_e r) + C_Y C'_{J1}(k_e r)] \\
& \times \sin \left(k'_e r - \frac{3}{4}\pi \right) \Big\} dr, \tag{58}
\end{aligned}$$

$$\begin{aligned}
\Gamma_3(\omega, \omega') &= \frac{\rho_e a^2}{\pi \sqrt{k_e k'_e}} \int_a^\infty [C_J C'_{J1}(k_e r) j_1(k'_e r) \\
&+ C_J C'_{Y1}(k_e r) y_1(k'_e r) \\
&+ C_Y C'_{J1}(k_e r) j_1(k'_e r) \\
&+ C_Y C'_{Y1}(k_e r) y_1(k'_e r)] dr, \tag{59}
\end{aligned}$$

$$\begin{aligned}
\Upsilon(\omega, \omega') &= \frac{\rho_e a^4}{\pi} \sqrt{k_e k'_e} \\
&\times \int_a^\infty \{ (C_J C'_J + C_Y C'_Y) \cos [r(k_e - k'_e)] \\
&- (C_J C'_Y + C_Y C'_J) \cos [r(k_e + k'_e)] \\
&- (C_J C'_Y - C_Y C'_J) \sin [r(k_e - k'_e)] \\
&+ (C_J C'_J - C_Y C'_Y) \sin [r(k_e + k'_e)] \} dr. \tag{60}
\end{aligned}$$

As it is explained in Paper I, $\Gamma(\omega, \omega')$ is a regular function of ω and ω' . Repeating the same calculation as in Paper I we obtain that

$$\langle \hat{\xi}_\omega, \hat{\xi}_{\omega'} \rangle = Q(\omega, \omega') + \frac{\rho_e a^4 v_{Ae}^2 k_e^2}{\omega} W(\omega, \omega') \delta(\omega - \omega'), \tag{61}$$

where $Q(\omega, \omega')$ is a regular function and

$$W(\omega, \omega') = (C_J C'_J + C_Y C'_Y) \cos [a(k_e - k'_e)]. \tag{62}$$

Using the same arguments as in Paper I we prove that $Q(\omega, \omega') \equiv 0$ and $W(\omega, \omega') \delta(\omega - \omega') = W(\omega, \omega) \delta(\omega - \omega')$. Then we obtain

$$q(\omega) = \frac{\rho_e a^4 v_{Ae}^2 k_e^2}{\omega} (C_J^2 + C_Y^2). \tag{63}$$

APPENDIX C AMPLITUDES OF FAST KINK MODES FOR SPECIFIC INITIAL CONDITIONS

In Paper I the evolution of an initial transverse displacement of the magnetic tube was studied. The radial variation of the initial disturbance outside the magnetic cylinder was taken as $\exp(-(r-a)^2/l^2)$, with l a prescribed length. In the present paper this external radial variation is a/r . We now derive expressions for the amplitudes $A_j^\pm(k)$ and $A_\omega^\pm(k)$ for a transverse perturbation whose initial radial distribution is

$\psi(r) = a/r$ for $r \geq a$. Note that for this type of perturbation we still use $\psi(r) = 1$ for $r \leq a$.

We start with the proper mode amplitudes $A_j^\pm(k)$, that are given by Equation (38) of Paper I with

$$\begin{aligned}
\mathcal{N}_j(k) &= a \xi_0 \sqrt{\pi} \Delta \omega_j \exp(-\Delta^2 k^2/4) J_1(k_i a) \\
&\times \left\{ \frac{\rho_i}{k_i^2} K_1(\kappa_e a) - \frac{\rho_e}{\kappa_e^2} \left[-\frac{\pi}{2} + \kappa_e a K_0(\kappa_e a) \right. \right. \\
&\left. \left. + \Psi_K(\kappa_e a) \right] \right\}, \tag{64}
\end{aligned}$$

where

$$\Psi_K(x) = \frac{\pi}{2} x [K_0(x) L_1(x) + K_1(x) L_0(x)]. \tag{65}$$

This function is introduced by Rosenheinrich (2014), p. 6, and appears when obtaining the primitive of $K_1(x)/x$, see Rosenheinrich (2014), p. 19. Furthermore, $L_0(x)$ and $L_1(x)$ are the modified Struve functions.

The denominator of Equation (38) of Paper I contains

$$\begin{aligned}
D_j(k) &= \frac{\rho_i K_1^2(\kappa_e a)}{2k_i^4} \{ k_i^2 a^2 J_0^2(k_i a) \\
&+ (k_i^2 a^2 - 2) J_1^2(k_i a) \} \\
&+ \frac{\rho_e J_1^2(k_i a)}{2\kappa_e^4} \{ -\kappa_e^2 a^2 K_0^2(\kappa_e a) \\
&+ (\kappa_e^2 a^2 + 2) K_1^2(\kappa_e a) \}. \tag{66}
\end{aligned}$$

To derive this result the primitive of $x K_1'^2(x)$ is required. We have used Equation (34) to express $K_1'(x)$ in terms of $K_0(x)$ and $K_1(x)$. Next, the primitive has been calculated with the help of expressions in Rosenheinrich (2014), pp. 143 and 160, with $I_0(x)$ and $I_1(x)$ replaced by $K_0(x)$ and $K_1(x)$.

Finally, Equation (42) of Paper I gives the amplitudes $A_\omega^\pm(k)$, where the numerator is

$$\begin{aligned}
\mathcal{N}_\omega(k) &= a \xi_0 \sqrt{\pi} \Delta \omega \exp(-\Delta^2 k^2/4) \\
&\times \left\{ \frac{\rho_i k_e^2 a^2}{k_i^2} J_1(k_i a) \right. \\
&+ \rho_e a^2 [C_J (1 - k_e a J_0(k_e a) - \Phi(k_e a)) \\
&\left. + C_Y (-k_e a Y_0(k_e a) - \Phi_Y(k_e a))] \right\}, \tag{67}
\end{aligned}$$

where the primitive of $J_1(x)/x$ is given in Rosenheinrich (2014), p. 19, in terms of the function

$$\Phi(x) = \frac{\pi}{2} x [J_1(x) \mathbf{H}_0(x) - J_0(x) \mathbf{H}_1(x)], \tag{68}$$

with $\mathbf{H}_0(x)$ and $\mathbf{H}_1(x)$ the Struve functions. The primitive of $Y_1(x)/x$ is derived in the same way by substituting $J_0(x)$ and $J_1(x)$ by $Y_0(x)$ and $Y_1(x)$ and $\Phi(x)$ by $\Phi_Y(x)$. This function is defined as

$$\Phi_Y(x) = \frac{\pi}{2} x [Y_1(x) \mathbf{H}_0(x) - Y_0(x) \mathbf{H}_1(x)]. \tag{69}$$

The numerical evaluation of the Struve and modified Struve functions has been done with the software developed by MacLeod (1996).

REFERENCES

- Abramowitz, M., & Stegun, I. A. 1964, *Handbook of Mathematical Functions with Formulas, Graphs, and Mathematical Tables* (10th ed.; New York: Dover)
- Andries, J., & Goossens, M. 2007, *PhPl*, **14**, 052101
- Anfinogentov, S., Nisticò, G., & Nakariakov, V. M. 2013, *A&A*, **560**, A107
- Antolin, P., & van Doorselaere, T. 2013, *A&A*, **555**, A74
- Aschwanden, M. J., Fletcher, L., Schrijver, C. J., & Alexander, D. 1999, *ApJ*, **520**, 880
- Bogdan, T. J., & Judge, P. G. 2006, *RSPTA*, **364**, 313
- Cally, P. S. 1986, *SoPh*, **103**, 277
- Cally, P. S. 2003, *SoPh*, **217**, 95
- Cooper, F. C., Nakariakov, V. M., & Tsiklauri, D. 2003a, *A&A*, **397**, 765
- Cooper, F. C., Nakariakov, V. M., & Williams, D. R. 2003b, *A&A*, **409**, 325
- De Moortel, I. 2009, *SSRv*, **149**, 65
- De Moortel, I., & Bradshaw, S. J. 2008, *SoPh*, **252**, 101
- De Moortel, I., & Nakariakov, V. M. 2012, *RSPTA*, **370**, 3193
- De Pontieu, B., Carlsson, M., Rouppe van der Voort, L. H. M., et al. 2012, *ApJL*, **752**, L12
- Edwin, P. M., & Roberts, B. 1983, *SoPh*, **88**, 179
- Jelínek, P., & Karlický, M. 2010, *ITPS*, **38**, 2243
- Jelínek, P., & Karlický, M. 2012, *A&A*, **537**, A46
- Jelínek, P., Karlický, M., & Murawski, K. 2012, *A&A*, **546**, A49
- Karlický, M., Mészárosová, H., & Jelínek, P. 2013, *A&A*, **550**, A1
- Katsiyannis, A. C., Williams, D. R., McAteer, R. T. J., et al. 2003, *A&A*, **406**, 709
- Lin, Y., Engvold, O., Rouppe van der Voort, L. H. M., & van Noort, M. 2007, *SoPh*, **246**, 65
- Liu, W., Ofman, L., Nitta, N. V., et al. 2012, *ApJ*, **753**, 52
- Liu, W., Title, A. M., Zhao, J., et al. 2011, *ApJL*, **736**, L13
- MacLeod, A. J. 1996, *ACM Trans. Math. Softw.*, **22**, 288
- Mészárosová, H., Dudík, J., Karlický, M., Madsen, F. R. H., & Sawant, H. S. 2013, *SoPh*, **283**, 473
- Mészárosová, H., Karlický, M., & Rybák, J. 2014, *ApJ*, **788**, 44
- Mészárosová, H., Karlický, M., & Rybák, J. 2011, *SoPh*, **273**, 393
- Mészárosová, H., Karlický, M., Rybák, J., & Jiříčka, K. 2009, *ApJL*, **697**, L108
- Murawski, K., & Roberts, B. 1993a, *SoPh*, **144**, 101
- Murawski, K., & Roberts, B. 1993b, *SoPh*, **145**, 65
- Nakariakov, V. M., Arber, T. D., Ault, C. E., et al. 2004, *MNRAS*, **349**, 705
- Nakariakov, V. M., Hornsey, C., & Melnikov, V. F. 2012, *ApJ*, **761**, 134
- Nakariakov, V. M., Ofman, L., Deluca, E. E., Roberts, B., & Davila, J. M. 1999, *Sci*, **285**, 862
- Nakariakov, V. M., Pascoe, D. J., & Arber, T. D. 2005, *SSRv*, **121**, 115
- Nakariakov, V. M., & Roberts, B. 1995, *SoPh*, **159**, 399
- Nakariakov, V. M., & Verwichte, E. 2005, *LRSF*, **2**, 3
- Nisticò, G., Nakariakov, V. M., & Verwichte, E. 2013, *A&A*, **552**, A57
- Nisticò, G., Pascoe, D. J., & Nakariakov, V. M. 2014, *A&A*, **569**, A12
- Ofman, L., Liu, W., Title, A., & Aschwanden, M. 2011, *ApJL*, **740**, L33
- Okamoto, T. J., & De Pontieu, B. 2011, *ApJL*, **736**, L24
- Okamoto, T. J., Tsuneta, S., Berger, T. E., et al. 2007, *Sci*, **318**, 1577
- Oliver, R., Ruderman, M. S., & Terradas, J. 2014, *ApJ*, **789**, 48
- Pascoe, D. J., Nakariakov, V. M., & Kupriyanova, E. G. 2013, *A&A*, **560**, A97
- Pascoe, D. J., Nakariakov, V. M., & Kupriyanova, E. G. 2014, *A&A*, **568**, A20
- Reznikova, V. E., Antolin, P., & van Doorselaere, T. 2014, *ApJ*, **785**, 86
- Roberts, B., Edwin, P. M., & Benz, A. O. 1984, *ApJ*, **279**, 857
- Rosenheinrich, W. 2014, *Tables of some indefinite integrals of Bessel functions* (<http://www.fh-jena.de/~rsh/Forschung/Stoer/besint.pdf>)
- Ruderman, M. S., & Erdélyi, R. 2009, *SSRv*, **149**, 199
- Ruderman, M. S., & Roberts, B. 2006, *JPIPh*, **72**, 285
- Selwa, M., Murawski, K., & Kowal, G. 2004, *A&A*, **422**, 1067
- Shen, Y., & Liu, Y. 2012, *ApJ*, **753**, 53
- Shen, Y.-D., Liu, Y., Su, J.-T., et al. 2013, *SoPh*, **288**, 585
- Tomczyk, S., & McIntosh, S. W. 2009, *ApJ*, **697**, 1384
- Tomczyk, S., McIntosh, S. W., Keil, S. L., et al. 2007, *Sci*, **317**, 1192
- Williams, D. R., Mathioudakis, M., Gallagher, P. T., et al. 2002, *MNRAS*, **336**, 747
- Williams, D. R., Phillips, K. J. H., Rudawy, P., et al. 2001, *MNRAS*, **326**, 428
- Yuan, D., Shen, Y., Liu, Y., et al. 2013, *A&A*, **554**, A144